International Journal of Hydrogen Energy 197 (2026) 152565

Contents lists available at ScienceDirect

International Journal of Hydrogen Energy

journal homepage: www.elsevier.com/locate/he

MOF-derived PdMn and PdCo bimetallic systems as bifunctional electrocatalysts for overall water splitting

Jordan Santiago Martinez [a], Inmaculada Márquez [b], Jaime Mazarío [a], Christian Wittee Lopes [c], Christian Cerezo-Navarrete [a], Gonzalo Egea [a], Giovanni Agostini [f], Eduardo Villalobos-Portillo [f], Otman Bazta [d,e], Susana Trasobares [d,e], Jose Juan Calvino [d,e], Juan José Calvente [b], José Luis Olloqui-Sariego [b,*], Pascual Oña-Burgos [a,**]

[a] Instituto de Tecnología Química, Universitat Politècnica de València-Consejo Superior de Investigaciones Científicas (UPV-CSIC), Avda. de Los Naranjos S/n, 46022, Valencia, Spain
[b] Departamento de Química Física, Universidad de Sevilla, Profesor García González 1, 41012, Sevilla, Spain
[c] Department of Chemistry, Federal University of Paraná (UFPR), Curitiba, 81531-980, Brazil
[d] División de Microscopía Electrónica de Los Servicios Centralizados de Investigación Científica y Tecnológica de La Universidad de Cádiz (DME-UCA), Facultad de Ciencias, Universidad de Cádiz, Campus Río San Pedro S/N, Puerto Real, 11510, Cádiz, Spain
[e] Departamento de Ciencia de Los Materiales e Ingeniería Metalúrgica y Química Inorgánica, Facultad de Ciencias, Universidad de Cádiz, Campus Río San Pedro S/N, Puerto Real, 11510, Cádiz, Spain
[f] ALBA Synchrotron Light Facility, Carrer de La Llum 2-26, Cerdanyola Del Vallès, Barcelona, 08290, Spain

ARTICLE INFO

Keywords:
MOF-Derived
Bimetallic nanoparticles
Nanomaterials characterization
Electrocatalytic water splitting
Bifunctional electrocatalyst

ABSTRACT

Bimetallic Metalorganic Framework (MOF)-derived PdCo and PdMn nanoparticles have been shown to be excellent bifunctional electrocatalysts for overall electrocatalytic alkaline water splitting. Through an innovative strategy combining a soft chemical (**Q**) transformation followed by pyrolysis (**T**) of **PdCo-MOF** and **PdMn-MOF** precursors, well-defined and uniformly distributed nanoparticles supported on N-doped graphitic carbon were synthesized (**PdCo-QT** and **PdMn-QT**, respectively). The influence of the first row transition metal into the bimetallic nanoparticles on the electrocatalytic activity for both electrocatalytic hydrogen evolution reaction (HER) and oxygen evolution reaction (OER) was assessed. Comprehensive characterization using TEM/STEM, PXRD, Raman, XAS and XPS revealed the ultimate structural and compositional features of the synthesized materials. Notably, the bimetallic PdCo-based catalyst demonstrated the best electrocatalytic performance, exhibiting the lowest Tafel slopes for both HER and OER processes, along with superior thermodynamic and kinetic metrics compared to the bimetallic PdMn and monometallic Pd nanoparticles. The exceptional catalytic activity of the **PdCo-QT** electrode competes with that of benchmark materials, attributed to a synergistic effect between Pd and the secondary metal (Co), likely forming **Pd–O(OH)–Co** active centers. Moreover, operando and after electrocatalysis characterizations of the electrodes validate the remarkable stability and efficiency of **PdCo-QT**, underscoring its potential for practical water-splitting applications.

1. Introduction

Hydrogen is increasingly seen as a promising solution to the growing demand for clean, renewable, and sustainable energy due to its zero-emission characteristics and high energy density [1–5]. In this context, electrochemical water splitting driven by renewable energy sources is an appealing method for producing "green" hydrogen [6–9]. Two main technologies are currently employed for industrial-scale hydrogen production via water splitting (WS): acidic water electrolyzers with polymer electrolyte membranes and alkaline water electrolyzers [10,11]. Water electrolysis (WE) is based on two semi-reactions, the hydrogen evolution reaction (HER) at the cathode and the oxygen evolution reaction (OER)

* Corresponding author.
** Corresponding author.
E-mail addresses: jlolloqui@us.es (J.L. Olloqui-Sariego), pasoabur@itq.upv.es (P. Oña-Burgos).

https://doi.org/10.1016/j.ijhydene.2025.152565
Received 11 August 2025; Received in revised form 14 October 2025; Accepted 12 November 2025
Available online 22 November 2025
0360-3199/© 2025 The Authors. Published by Elsevier Ltd on behalf of Hydrogen Energy Publications LLC. This is an open access article under the CC BY-NC-ND license (http://creativecommons.org/licenses/by-nc-nd/4.0/).

at the anode, leading to hydrogen and oxygen gases formation, respectively. In standard conditions, the free Gibbs energy ($\Delta_r G^0$) associated with the water splitting reaction is 237.2 kJ mol^{-1}, corresponding to a standard cell potential of $E^0 = 1.23$ V (pH 0) [12,13]. Therefore, water splitting is a difficult reaction that is usually thermodynamic- and kinetically hampered by the OER half-reaction [14–16]. Consequently, decreasing the overpotential associated with the OER while maintaining the thermodynamic requirements for the HER is a major challenge for a feasible WS technology. Furthermore, researching effective bifunctional electrocatalysts for overall water splitting is crucial. While platinum-based materials are the benchmark catalysts for HER, they are not effective for OER. Conversely, iridium and ruthenium oxides are excellent materials for electrocatalytic OER but are largely inefficient for HER [17]. Moreover, the high cost and scarcity of these noble metals further limit their widespread use [6,8,18]. A promising approach to develop high-performing bifunctional catalysts for both HER and OER involves combining first-row transition metals such as nickel, cobalt, or manganese with noble metals [19–23]. In that sense, recent studies indicate that the generation of an active phase combining a second metal with palladium species seems an auspicious alternative, since this heterometallic phase can improve the OER catalytic activity *versus* homometallic systems, preserving the typical HER activity observed in Pd-based electrocatalysts. Specifically, heterometallic M–M′O_xH_y intermediates [24–31] are believed to enhance OER activity compared to homometallic systems, thanks to charge delocalization between metal centers [25]. By balancing the rates of first raw transition metal dissolution and re-deposition on a MO_xH_y host, dynamically stable active sites can be established, which improves OER activity. The interaction between the noble metal and the MOxHy host is crucial for controlling the number of active sites at the electrode/solution interface, leading to enhanced electrocatalytic performances [25].

Besides, high-porosity carbon materials are ideal supports for bifunctional electrocatalysts due to their high conductivity, large surface area, tunable porosity, affordability, and strong corrosion resistance [32]. Although pyrolysis of carbon precursors such as polymeric aerogels and organic materials has been explored, disordered activated carbon faces limitations from uneven pore distribution, relatively low surface area and challenges in achieving effective heteroatom doping. In that sense, the optimization of carbon structures with high surface area, large pore volume, and stable electrocatalytic activity is crucial overall performance [33–35]. In light of this, MOF-derived materials have emerged as a promising strategy to simultaneously promote the formation of bifunctional metal electroactive centers as well as achieve a promising carbon structures. By treating MOF precursors with chemical modifications and heat, researchers can tailor their structure for improved bifunctional character, conductivity, active sites accessibility, and mass transfer [36–39].

In that context, we recently developed a novel methodology to chemically transform a **PdFe-MOF** into Fe-doped Pd nanoparticles (NPs) supported on clusters of FeOx@C (PdFe@FeOx-C) [40]. Compared to other strategies, this soft synthesis method enables a better tailoring of the material's properties, achieving well-defined and distributed small NPs (2.3 nm), despite the material having 35 wt% metal loading. From nitrobenzene, the *in situ* aniline generation in the presence of 5 bar of H_2 at room temperature provides a controlled, slow supply of amine, resulting in a reproducible material that combines metallic NPs and an FeOx-doped graphitic support. Interestingly, this PdFe electrocatalyst could be used as a bifunctional electrocatalysts for overall water splitting. The ultrasmall PdFe-NP proved to have a high number of Fe–Pd interactions, making it an excellent candidate for HER, while the nanometric iron oxide was effective for OER. Meanwhile, we have recently combined that strategy with a pyrolytic treatment, resulting in the synthesis of efficient MOF-derived PdCo and PdMn bimetallic nanoparticles with enhanced stability and resistance to leaching (denoted as **PdCo-QT** and **PdMn-QT**) [41,42].

In this line, looking at our previously reported findings related to the PdFe-derived nanocomposite and the PdCo and PdMn systems, the latter appeared as the perfect candidates to be used as electrodes for the overall water splitting reaction. Therefore, their electrocatalytic performances were evaluated in this work by testing their HER and OER activity and long-term stability. Notably, **PdCo-QT**-based electrodes exhibit outstanding performances as bifunctional catalysts for electrocatalytic water splitting under basic conditions. Additionally, a thorough characterization of the electrodes before, during, and after electrocatalysis provides valuable insights for the future design of analogous efficient bifunctional electrocatalysts for sustainable hydrogen production.

2. Results and discussion

2.1. Structural characterization of PdM-QT-based electrocatalysts

In this work, electrodes based on well-defined Pd-based bimetallic nanoparticles supported on a N-doped carbon are developed. First, fresh materials were obtained from PdCo and PdMn MOFs precursors using a soft chemical treatment using in-situ generated aniline (from nitrobenzene) and H_2, followed by pyrolysis [42]. Then, the resulting PdM-QT materials (M = Co or Mn) were dispersed in an alcoholic Nafion suspension, forming the catalytic composite for further deposition on the graphite electrodes. To explore the atomic distribution and structural properties of the so-called **PdCo-QT@Nafion** and **PdMn-QT@Nafion** composites, high-resolution electron microscopy imaging (HREM and HAADF), powder X-ray diffraction (PXRD), X-ray photoelectron spectroscopy (XPS), and Raman analysis were performed (*see SI, Section II Catalyst characterization and Section V Additional characterization*). Fig. 1 provides a summary of the microscopy characterization of both composites. Notably, nanoparticle size, composition and crystalline structures within the nanocomposites remain unchanged compared to the previously reported pure materials [42]. Precisely, the **PdCo-QT@Nafion** and **PdMn-QT@Nafion** composites still present well-defined and distributed carbon-supported nanoparticles with average size of 17.0 ± 5.4 nm and 12.1 ± 3.8 nm, respectively, and the STEM XEDS maps provided in Fig. S7 prove an intimate metal mixture.

Furthermore, the PXRD patterns of **PdCo-QT@Nafion** composite in Fig. 2a showed the presence of two face-centered cubic (*fcc*) $Pd_{0.7}Co_{0.3}$ and $Pd_{0.9}Co_{0.1}$ crystal systems together with small proportions of monometallic phases, while PXRD patterns of **PdMn-QT@Nafion** reveals a tetragonal Pd_1Mn_1 crystal system [42]. Similarly, the graphitic carbon nature of the catalysts depicted by the Raman spectra in Fig. S2b remains unchanged before and after the incorporation of Nafion. Note the presence of the peaks corresponding to CoO_x species in the **PdCo-QT-based** materials. The signals at 631 cm^{-1} and 672 cm^{-1} correspond to shifted F_{2g} and A_{1g} Co_3O_4 transitions, likely due to Pd–Co-O_x, or Pd-O_x-Co interactions [42,43]. Additionally, the typical graphitic carbon G band appears around 1589 cm^{-1}, with the I_D/I_G ratio suggesting a low carbon order in both materials [44,45].

Furthermore, the electronic states of Pd, C, and N in both freshly prepared composites were analysed by XPS and their corresponding spectra are depicted in Fig. 3. First, regarding the C*1s* XP region (Fig. 3a), apart from the typical signals from sp^2 carbon (graphitic), sp^3 carbon (C – C, C – H), C – O and C – N, and O – C═O, already identified in our previous work [42], the Nafion contributions can be observed at higher binding energies (B.E). In particular, a signal at ca. 292 eV, corresponds to the main Nafion's structural units (– CF_2 – and – CF – O) [46,47]. Moreover, while addressing the fitting of the C*1s*, it became necessary to introduce an additional component at a BE lower than that of the graphitic peak, previously associated with C atoms close to vacancy-like defects [48]. Alternatively, a differential charging effect of over a fraction of the carbon might account for this effect. In the Pd*3d* XP region (Fig. 3b), signals characteristic of $Pd^0 3d_{5/2}$ appear at 335.1 eV for **PdCo-QT@Nafion** and **PdMn-QT@Nafion**. Also, surface oxidized Pd

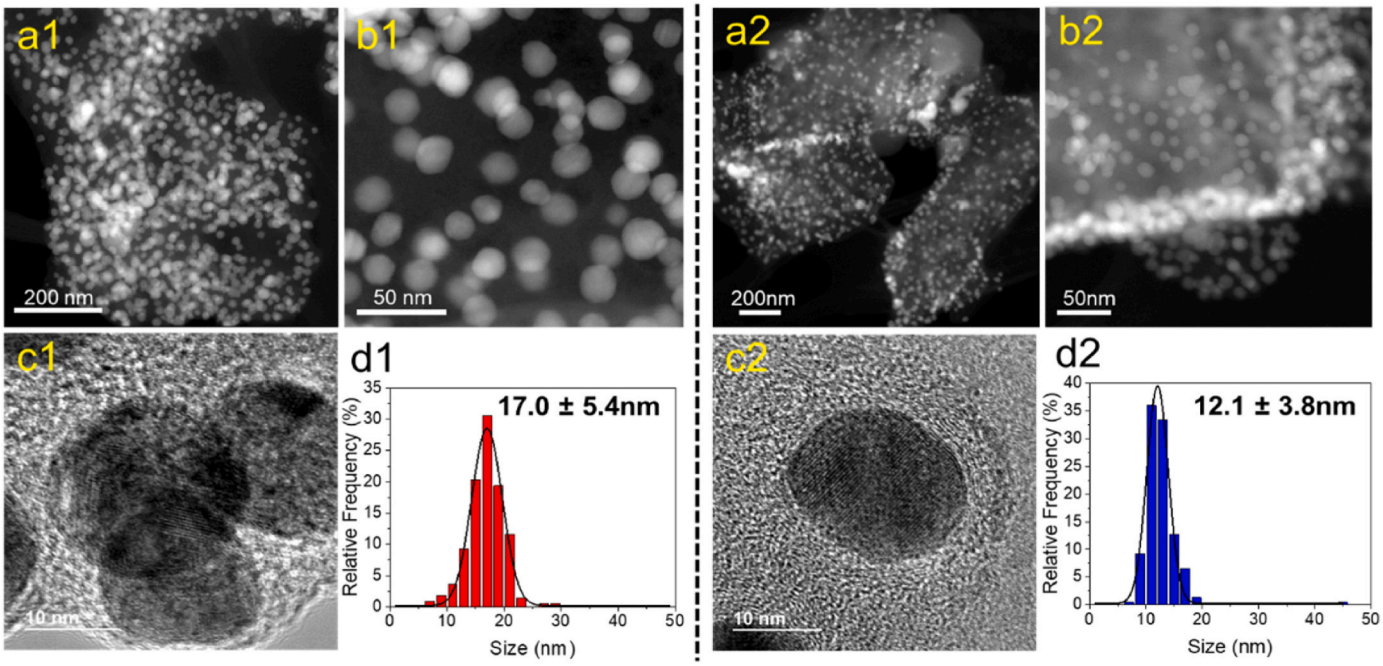

Fig. 1. Electron microscopy characterization of **PdCo-QT@Nafion** (panel 1) and **PdMn-QT@Nafion** (panel 2) composites. Their representative (a, b) HAADF-STEM, (c) HR-TEM images and, (d) nanoparticle size distribution.

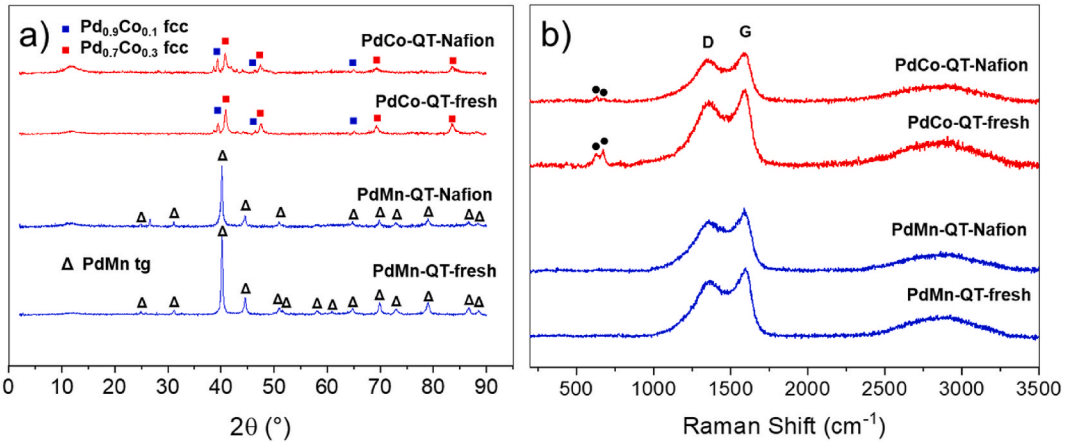

Fig. 2. (a) XRD patterns and (b) Raman spectra of PdM-QT fresh and with Nafion, PdMn (blue), PdCo (red). (For interpretation of the references to color in this figure legend, the reader is referred to the Web version of this article.)

peaks at higher B.E. (337.2–336.7 eV) could easily be introduced in the fitting in both cases. Additionally, one last peak stood out in the case of **PdMn-QT@Nafion** at 339.2 eV, suggesting either a differential charging effect of a Pd fraction or the distortion of its environment by the F from Nafion [49–51]. Unfortunately, upon mixing with Nafion, the main XP regions for the Co and Mn elements became weaker and very close to the spectrometer's quantification limit. Although these elements could be detected by XPS, no peak fitting or quantification was done out of precaution (Fig. S9). Then, the N*1s* fitting (Fig. 3c) reveals in the PdMn and PdCo composites a nitrogen signal at ca. 400.7 eV, as found in our previous works after submitting the MOF to the combination of chemical and thermal treatments [41,42]. This signal, according to specialized literature, should be associated with graphitic nitrogen (isolated N defect), pyrrolic nitrogen or nitrogen coordinated to metal [52]. The increase in peak width (FWHM) observed in **PdCo-QT** with Nafion (3.6 eV) compared to the material without Nafion (2.8 eV) [42] suggests a more heterogeneous nitrogen environment, which may be unresolved due to the quality of the spectra. In addition, **PdMn-QT@Nafion** displays a pyridine signal at 399.0 eV. However, this B.E. is too high for free pyridine and too low to be associated with pyridine coordinated to Pd. Especially, if considering the values we previously reported in the parent MOFs and Nafion-free composites (ca. 398.5 and 400.3 eV, respectively) [42]. Thus, free pyridine seems losing negative charge due to an interaction with an unidentified component from the catalyst matrix, perhaps becoming protonated, hydrogen bonded, or chemically coordinated, pushing it toward a higher B.E. The fitting constraints and the charge referencing methodology used in these analyses can be found in the Supporting Information *Section II-Catalyst characterization (XPS)* Table S1 [42,53–55].

2.2. Electrochemical characterization of PdM-QT based electrodes

2.2.1. Electrochemical activation of the PdM-QT-based electrodes

Electrodes based on the deposited catalytic composites typically require an electrochemical activation process. Thus, prior to the assessment of the electrocatalytic properties of the bimetallic

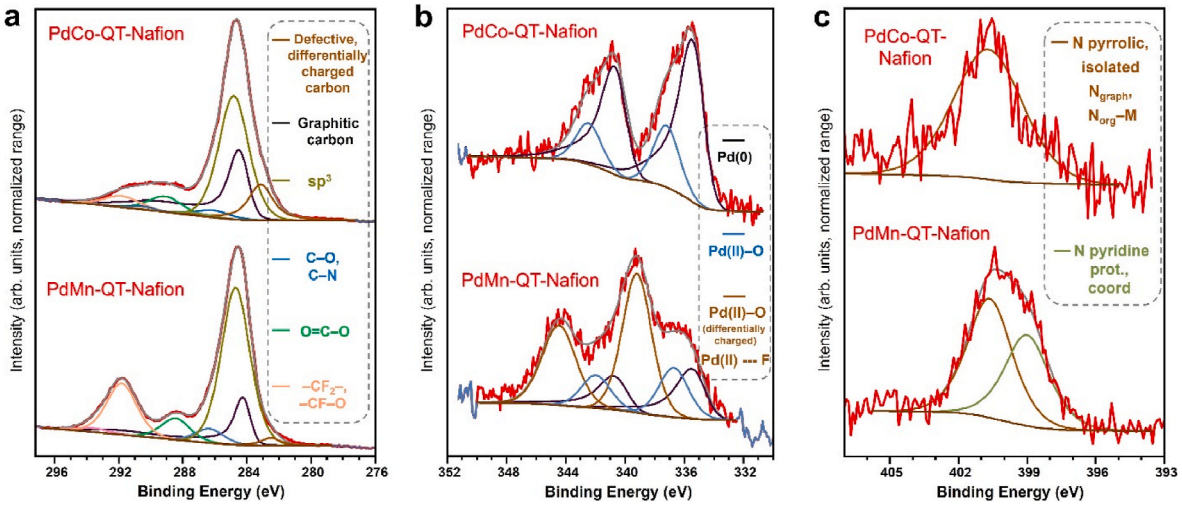

Fig. 3. (a) C*1s*, (b) Pd*3d*, and (c) N*1s* XPS regions of PdM-QT materials upon mixing with Nafion (X = Co or Mn).

nanoparticles for both HER and OER in an alkaline medium, the prepared electrodes were electrochemically activated by potentiostatic polarization by applying a fixed potential where the electrocatalytic reaction occurs. Specifically, the electrodes (**PdCo-QT@Nafion** and **PdMn-QT@Nafion**) were subjected to a potential of - 0.08 V vs RHE (Reversible Hydrogen Electrode) for applying for HER. In comparison, for OER electrodes the electroactivation was performed at 1.72 V vs. RHE. The activation was allowed to proceed until the linear scan voltammograms became stationary, typically lasting 45 min. Fig. 4 illustrates a comparison between the initial voltammetric responses and those of the activated electrodes for the different materials and reactions (i.e. HER and OER). Irrespective of the applied potential, the electrochemical activation leads to a significant increase in the capacitive current associated with the charge of the double layer of the electrode-solution interface, which ultimately implies an increase in the electrochemically active surface area (ECSA). Specifically, the ECSA values were calculated from the double layer capacitance of the current electrode (C_{dl}), obtained from the non-Faradaic voltammetric current at different scan rates (Fig. S1), and the specific capacitance (C_s) of a smooth planar pyrolytic edge graphite electrode (*see SI Section III Electrochemical Measurements*). Notably, the estimated ECSA of the activated electrodes strongly differs between materials, the **PdMn-QT@Nafion** value being three times higher than the corresponding **PdCo-QT@Nafion** (Fig. 4f). In addition, the ECSA obtained for the activated electrodes also depends on the potential applied during the activation. Indeed, the ECSAs achieved for the electrodes polarized at highly negative potentials are significantly higher than those activated at positive potentials. This is typically justified in terms of a different structural, compositional, and/or morphological reconstruction of the interphase during the activation [31].

In addition, the ECSA increase of the different electrodes parallels with an increase of both the faradaic current associated with the redox conversion involving the metal active centers, and the electrocatalytic current of both the electrocatalytic oxygen and hydrogen evolution. In particular, the cyclic voltammogram of an activated **PdCo-QT**-based electrode in the high potential window displays two poorly defined voltametric waves with midpoint potentials at 1.09 V and 1.40 V vs. RHE (Fig. 4b), which can be ascribed to the monoelectronic redox conversion Co(II)/Co(III) and Co(III)/Co(IV), following with an increase of the current associated with the electrocatalytic water oxidation. On the contrary, an activated **PdMn-QT**-based electrode by anodic polarization exhibits a cyclic voltammogram characteristic of supercapacitor behavior, consisting of a high capacitive current and the absence of redox conversion. Moreover, both cyclic voltammograms obtained for PdM-QT@Nafion electrodes after activation at negative potential are characterized by the pronounced electrocatalytic branches associated with the water reduction, which anticipates a high HER activity, and the oxidative desorption waves of the generated hydrogen, both processes likely involving the Pd metal sites.

2.2.2. *Electrocatalytic HER and OER activity of the activated PdM-QT-based electrodes*

The electrocatalytic activities of PdM-QT nanoparticles for alkaline HER and OER were assessed by rotating disk voltammetry. Fig. 5 shows the linear sweep voltammograms acquired at a scan rate of 5 mV s^{-1} and 1500 rpm of rotation rate obtained for the activated PdM-QT-based electrodes in 1 M KOH. Also, The HER and OER polarization curves of a modified electrode based on carbon-supported monometallic palladium nanoparticles (*see SI Section II-Catalyst Characterization **Pd-QT** reference material*) were also measured to evaluate the effect of introducing a second transition metal on Pd nanoparticles on the electrocatalytic activity for alkaline water splitting. First, an analysis of the HER polarization curves (Fig. 5a) reveals that the electrocatalytic branch commences at a lower onset potential for the **PdCo-QT** and **PdMn-QT**-based electrodes (−25 mV and −58 mV vs. RHE) compared to that obtained for the monometallic **Pd-QT** nanocomposite (−95 mV). Notably, the overpotential value at 10 mA cm^{-2}, defined as $\eta = E\text{-}E^0$ (with $E^0_{H^+/H_2} = 0$ V *vs.* RHE), of **PdCo-QT** and **PdMn-QT** based electrodes are also markedly lower than that of **Pd-QT**, with values of −48 mV and −97 mV in the case of the cobalt-doped and manganese-doped materials, respectively, and −141°mV in the case of the monometallic reference (Table 1), indicating a favored HER kinetics in the bimetallic systems, most notably for the **PdCo-QT@Nafion**-based electrode. To get insight into the HER mechanism through bimetallic PdM interfaces, we estimated the Tafel slopes obtained from the corresponding Tafel plots of the logarithm of the steady state currents against overpotential at high enough overpotential (Fig. 5d and Table 1). Notably, the Co-doped material yields the lowest slope (70 mV dec^{-1}) compared to those obtained in the Mn-doped and monometallic Pd materials with Tafel slopes of 145 mV dec^{-1} and 185 mV dec^{-1}, respectively. These results agree with previous works that reported higher activity of bimetallic electrocatalysts for HER in alkaline media [56–58]. From a mechanistic perspective, the values of the Tafel slope provide details about the rate-determining step (RDS) of the water reduction process. Accordingly, HER reaction involves two main steps: i) Proton adsorption via Volmer reaction by an initial discharge reaction, with a Tafel slope of 120 mV dec^{-1}; and ii) Hydrogen molecule release via Heyrovsky reaction or, electrochemical desorption reaction (Heyrovsky reaction) or homogeneous chemical desorption by a recombination reaction (Tafel

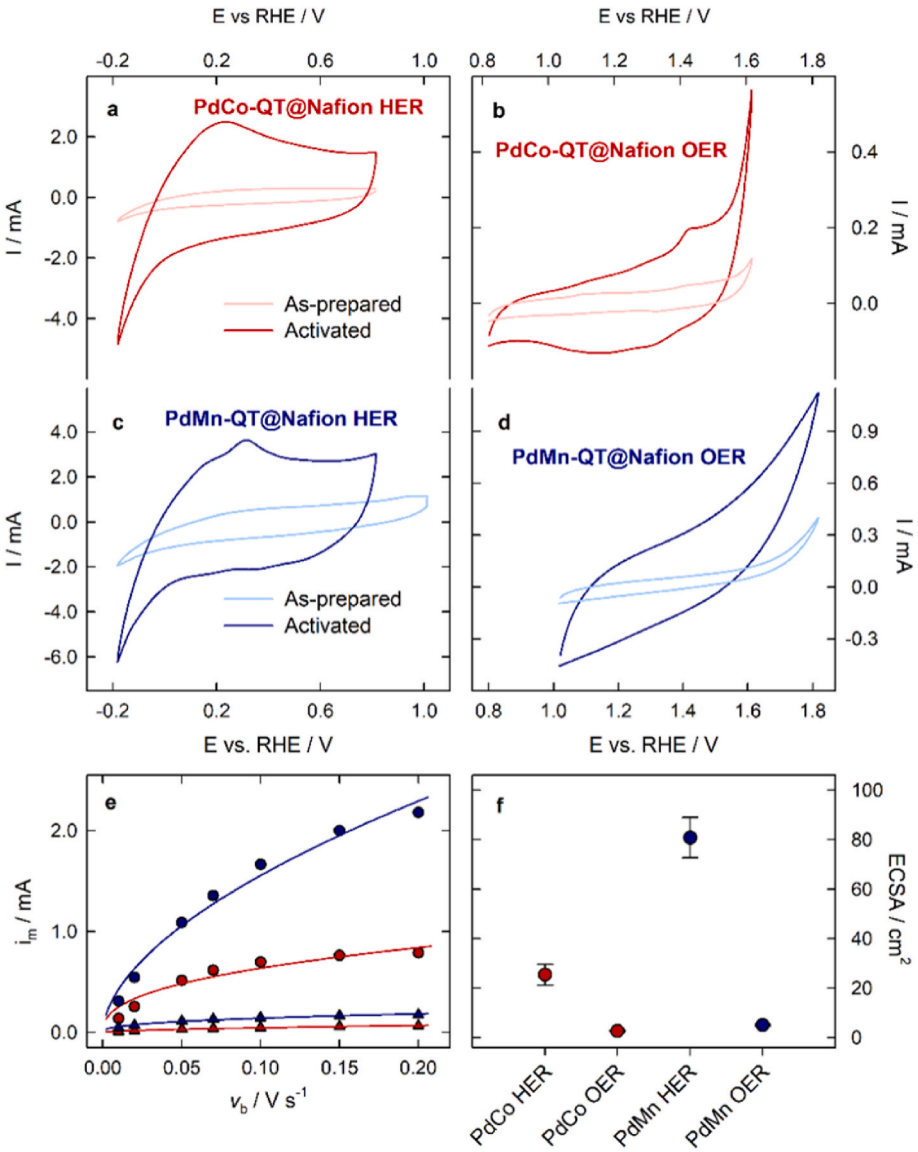

Fig. 4. (a–d) Cyclic voltammograms recorded at 50 mV s^{-1} in a deaerated 1 M KOH aqueous solution at 25 °C of a pyrolytic graphite electrode modified with **PdCo-QT@Nafion** (upper panel) and **PdMn-QT@Nafion** (lower panel) composites before and after being subjected to an electrochemical activation at - 0.08 V and 1.72 V *vs.* RHE for using in the HER (left panels) and OER (right panels) processes, respectively. (e) Average non-Faradaic current at different scan rates and (f) ECSA values of the above-mentioned electrodes (PdCo and PdMn composites in red and blue color, respectively) after being activated for HER (circle symbols) and OER (triangle symbols) processes. Solid lines in panel *e* correspond to experimental data fits employing equation 3 (*see SI*). (For interpretation of the references to color in this figure legend, the reader is referred to the Web version of this article.)

reaction), with Tafel slopes of 40 or 30 mV dec^{-1}, respectively (see Table S2) [59]. Accordingly, the Tafel slope values higher than 120 mV dec^{-1} obtained for **Pd-QT** and **PdMn-QT** are consistent with a slow discharge reaction involving an additional hydrogen adsorption step into the metal bulk, being the RDS the Volmer reaction [56,60–62]. On the other hand, the lower Tafel slope value of the **PdCo-QT** nanomaterial (with a value of ~ 70 mV dec^{-1}) agrees with a slow desorption reaction, being the RDS the electrochemical desorption step with generation of molecular hydrogen. The diminution on the Tafel slopes on bimetallic based materials points to a clear effect of the incorporation of the second metal into the HER activity, which we speculate may arise from a synergistic electronic interaction between the metallic species of the composite. It has been previously demonstrated, both by the experimental and DFT studies, that the relation between HER exchange current density in alkaline medium and H-binding energy values can be correlated via a volcano type of relationship [58,63,64]. Therefore, the superb HER kinetics at alkaline pH for the bimetallic material can be attributed to the hybrid nature of the catalyst that has an active component for water dissociation (metal transition and their oxides), thus promoting the proton adsorption which ultimately may increase the HER activity of its monometallic counterpart [31,65]. In addition, the significantly better HER kinetics of **PdCo-QT** nanomaterial can be explained in terms of the compact and low overlapping of cobalt with hydrogen, which it is expected to boost the HER reaction [66]. Finally, to compare their intrinsic electrocatalytic HER activity, their specific-mass activities (SMA) were determined by normalizing the electrocatalytic density current to the palladium loading (inset Fig. 5a). At a potential value of −0.10 V, the **PdCo-QT** nanomaterial exhibits an SMA value 3-fold higher than the corresponding for **Pd-QT** and **PdMn-QT** nanomaterials. Indeed, it is observed that the **PdCo-QT** bimetallic nanoparticles display a significantly higher SMA within the entire tested potential range (Fig. S4a). In comparison, the **PdMn-QT** based electrode exhibits slightly higher SMA than monometallic **Pd-QT**-electrodes. Altogether, these results reveal the outperforming

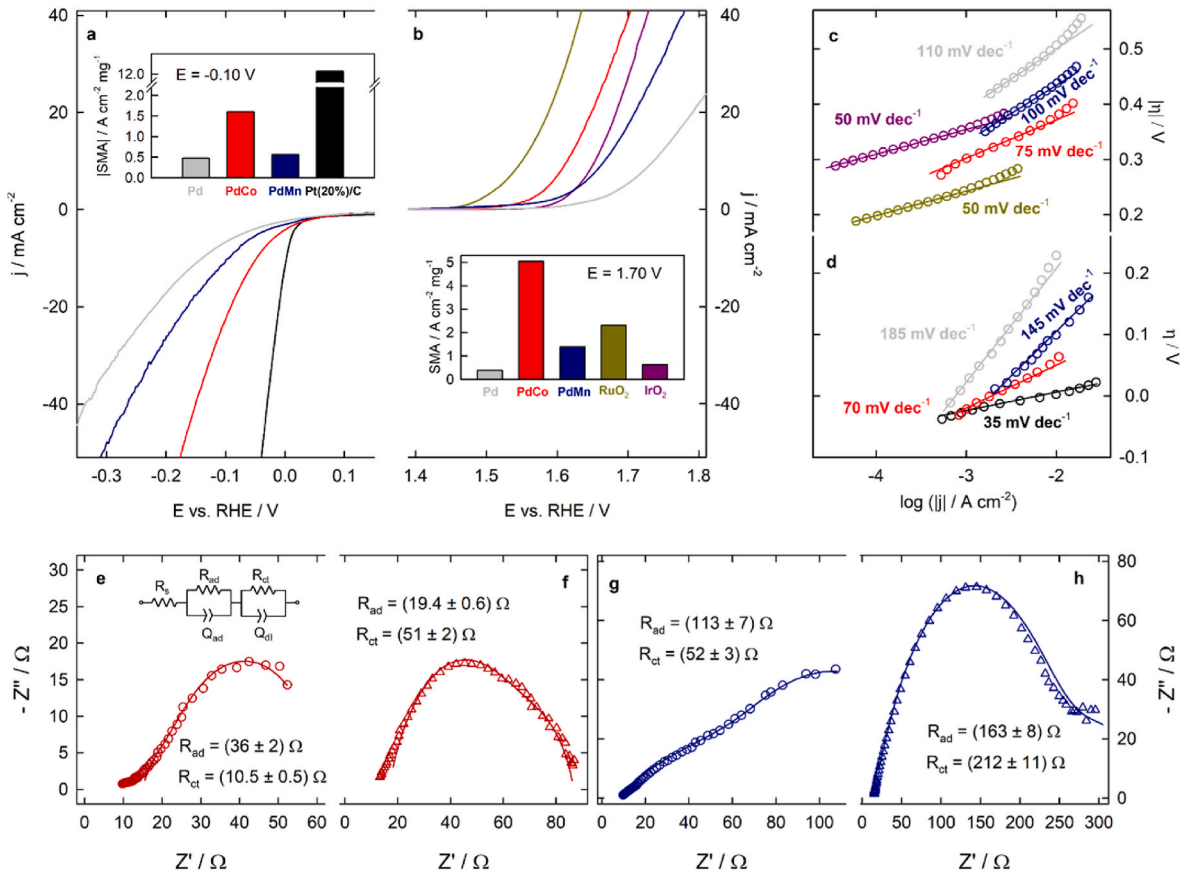

Fig. 5. (a) HER and (b) OER polarization curves recorded at 5 mV s^{-1} and 1500 rpm in a deaerated 1 M KOH aqueous solution at 25 °C of a pyrolytic graphite electrode coated with the **PdCo-QT@Nafion** (blue line), **PdMn-QT@Nafion** (red line) and **Pd-QT@Nafion** (grey line) composites and the corresponding benchmarking in the HER (Pt(20 %)/C – black line) and OER (RuO_2 – yellow line- and IrO_2 -purple line-) potential region. In the inset plots are depicted their corresponding specific-mass activity at the indicated potential. (c) OER and (d) HER steady-state Tafel plots of the above-mentioned electrodes. Nyquist plots of the (e) **PdCo-QT@Nafion** composite at −0.09 V and (f) 1.61 V, and (g) **PdMn-QT@Nafion** composite at −0.04 V and (h) 1.63 V. Solid lines in panels *e-h* correspond to experimental data fits employing a $R_s(R_{ad}Q_{ad})(R_{ct}Q_{dl})$ equivalent circuit and the indicated values of R_{ad} and R_{ct}. (For interpretation of the references to color in this figure legend, the reader is referred to the Web version of this article.)

electrocatalytic activity of bimetallic nanoparticles for HER in an alkaline medium. This can be justified in terms of a synergetic effect induced by M − Pd interaction [31]. Indeed, it is well recognized that metal alloys consisting of a noble metal (-*d*-electron number greater than -*d*-orbital number) and a non-noble transition metal (with unpaired *d*-electrons and unfilled *d*-orbital) improve the catalytic activity of the precious metal by changing charge distribution (see below) [67].

On the other hand, a comparison of the OER polarization curves of bimetallic PdM-QT nanoparticles at an alkaline medium with those of solely Pd nanoparticles is depicted in Fig. 5b. Interestingly, the electrocatalytic OER activities of the PdM-QT-based electrodes are markedly better than the monometallic Pd nanoparticles, being superior for the PdCo nanoparticle catalyst. This result indicates that the transition metal in the bimetallic nanoparticles can mediate the water oxidation reaction, thereby bringing forward its onset potential in the order of 1.56 V > 1.59 V > 1.66 V for the **PdCo-QT**, **PdMn-QT** and **Pd-QT**-based electrodes, respectively. In addition, Pd, PdCo and PdMn, nanoparticles display Tafel slopes of 110 mV dec^{-1}, 75 mV dec^{-1} and 100 mV dec^{-1}, respectively, indicating that **PdCo-QT** exhibits superb OER kinetics. For metal transition mediated OER follows the Krasil'shcikov path for alkaline electrolyte (Table S2) [68], which involves four steps where water molecules are adsorbed onto the reactive sites through an electrooxidation process, forming the M − OH species which then undergoes proton coupling and electron removal to form M−O intermediate that reacts with another water molecule to form M-OOH. Finally, M-OOH is oxidized by an electron transfer process to release O_2 and restore the initial metal active site. In this case, the obtained Tafel slope value also sheds light on the reaction mechanism's rate determining step. Accordingly, the RDS for **PdMn-QT** and **Pd-QT** materials corresponds primary discharge of OH^- ions leading to the hydroxyl adsorption (Tafel slope of 120 mV dec^{-1}), whilst in material (Tafel slope of 60 mV dec^{-1}), the RDS is probably related to the formation of oxide species (M−O) from the chemisorption of hydroxide (M−OH). This superior OER activity of the bimetallic **PdCo-QT** nanomaterials might be tentatively ascribed to the formation of M_1-O(OH)-M_2 bimetallic intersections charge that provokes the delocalization between metal centers (see below). This would lead to a higher number of active sites but also their stabilization, where the oxygen-oxygen bond formation could take place preferably through bimetallic centers, which ultimately improves the OER activity of these materials in alkaline media [25]. On the other hand, the slightly OER kinetic improvement by incorporating Mn can be attribute to the strongly low stability of the Mn^{3+} redox species, which is the active phase of the OER in MnO_2 type electrocatalysts. In addition, the specific-mass activity of PdCo and PdMn NPs, both determined by the normalization of current density with the non-palladium metal loadings (Table S3), are 13 and 4-fold higher at 1.70 V than that corresponding to the monometallic Pd NPs, respectively (Fig. 5b inset).

Furthermore, for comparative purposes, we benchmarked the electrocatalytic performance of the PdM-QT bimetallic composites with that corresponding to Pt(20 wt%)/C catalyst in HER, and IrO_2 and RuO_2 catalysts in OER (Insets in Fig. 5a and b). Firstly, we compared the HER and OER specific-mass activities of the bimetallic materials with the

Table 1
Comparative chart of the overpotentials (η_{10}) and Tafel slopes (TS) from HER and OER polarization curves of PdM-QT materials and the corresponding benchmarking.

	HER		OER	
Catalyst	**η_{10} / mV**	**TS / mV dec^{-1}**	**η_{10} / mV**	**TS / mV dec^{-1}**
Pd-QT	-141 ± 10	185 ± 15 (R^2 = 0.997)	507 ± 15	110 ± 15 (R^2 = 0.999)
PdCo-QT	-48 ± 5	70 ± 5 (R^2 = 0.999)	385 ± 15	75 ± 5 (R^2 = 0.998)
PdMn-QT	-97 ± 10	145 ± 15 (R^2 = 0.994)	438 ± 15	100 ± 15 (R^2 = 0.998)
Pt(20%)/C	6 ± 5	35 ± 5 (R^2 = 0.989)	-	-
RuO_2	-	-	321 ± 15	50 ± 5 (R^2 = 0.994)
IrO_2	-	-	424 ± 15	50 ± 5 (R^2 = 0.993)

η_{10}: overpotential at ±10 mA cm^{-2} from the OER and HER polarization curve, respectively.

corresponding benchmarking catalysts (Pt/C for HER and IrO_2, RuO_2 for OER). Inset in Fig. 5a reveals that the Pt(20 wt%)/C electrode performs greater specific-mass HER activities, at potential of −100 mV, than the PdM-QT bimetallic materials. In the OER region, the specific-mass activity at 1.70 V of the **PdCo-QT** bimetallic material is greater than those reported for RuO_2 and the IrO_2. Even the **PdMn-QT** specific-mass activity is higher than the IrO_2 benchmarking value, considered one of the most efficient OER electrocatalysts in alkaline medium [69].

Additionally, an electrochemical impedance spectroscopy analysis was conducted on the bimetallic composites at potential values, where the HER (−0.09 V and −0.04 V for **PdCo-QT** and **PdMn-QT**, respectively) and OER (1.61 V and 1.63 V for **PdCo-QT** and **PdMn-QT**, respectively) processes occur. The corresponding Nyquist spectra both agree with the overlapping of two semicircles, in which the intercept of the semicircle at high frequency with the *x*-axis is above 0 Ω. This is ascribed to an equivalent circuit consisting of a serial connection of a resistance (R) and two components, each formed by a parallel between a constant phase element (Q) and a resistance [70]. These represent the ohmic resistance (R_s), the proton/hydroxyl adsorption (Q_{ad} and R_{ad}) and the faradaic process (Q_{dl} and R_{ct}) (Inset Fig. 5e). Both the adsorption resistance and the resistance associated with the faradaic process for the **PdCo-QT** composite at HER potential region as well as OER region exhibit lower values than the corresponding for the **PdMn-QT** one, pointing to a more favored electrocatalysis processes by the PdCo bimetallic material in accordance with the voltammetric results. These results evidence that **PdCo-QT** catalyzes the water splitting process more efficiently than **PdMn-QT**.

2.3. Structural characterization of the activated PdCo-QT-based electrodes during and after catalytic reaction

Up to now, fresh electrodes have been structurally elucidated, and the electrocatalytic activity has been evaluated. These results pointed to the exciting behavior of the **PdCo-QT**-modified electrodes. To complement this view, the present section gathers the results of an ex-situ structural characterization of the **PdCo-QT**-based electrodes after electrocatalytic reactions by XRD, Raman, electron microscopy, XPS, Raman and XAS operando. Besides, structural analysis was also performed on the used PdMn-QT electrodes. However, considering the lower activity of this material, we focused mainly on the PdCo-based electrodes. The corresponding results for the **PdMn-QT** electrodes are provided in the Supporting Information (Fig. S11–S15 and Table S6-7).

Fig. 6 depicts the electron microscopy characterization of **PdCo-QT** electrodes after the OER and HER processes. Note how the **PdCo-QT** electrode presents a well-distributed nanoparticle population with an average size of 17.9 ± 6.2 nm, comparable to that of the fresh material (17.0 ± 5.4 nm). Besides, after the OER, the material also shows well distributed nanoparticles, but the size distribution reveals two differently sized nanoparticle populations with an average of 12.2 ± 4.8 nm and 20.1 ± 4.3 nm. As a reminder, the **PdCo-QT** composite is based on carbon-supported PdCo fcc bimetallic nanoparticles with two different compositions ($Pd_{0.7}Co_{0.3}$ and $Pd_{0.9}Co_{0.1}$). Thus, the size modification observed following the OER suggests a different evolution of the two types of PdCo NPs under working conditions.

With the idea of further understanding the previous observations and complementing, the stability studies of the **PdCo-QT** composite after the electrocatalytic process, Fig. 7 and Table S4 depict the corresponding PXRD analyses. All the resulting diffractograms show patterns similar to that of the fresh nanocomposites, with the signals of $Pd_{0.7}Co_{0.3}$ and $Pd_{0.9}Co_{0.1}$ fcc structures, as discussed in a previous section. On the one hand, after HER catalysis, crystal size values are very close to the fresh material composite, which confirms the material stability in this process, echoing the HAADF observations. On the other hand, after the OER process, the relative intensity of the signals between both fcc crystal

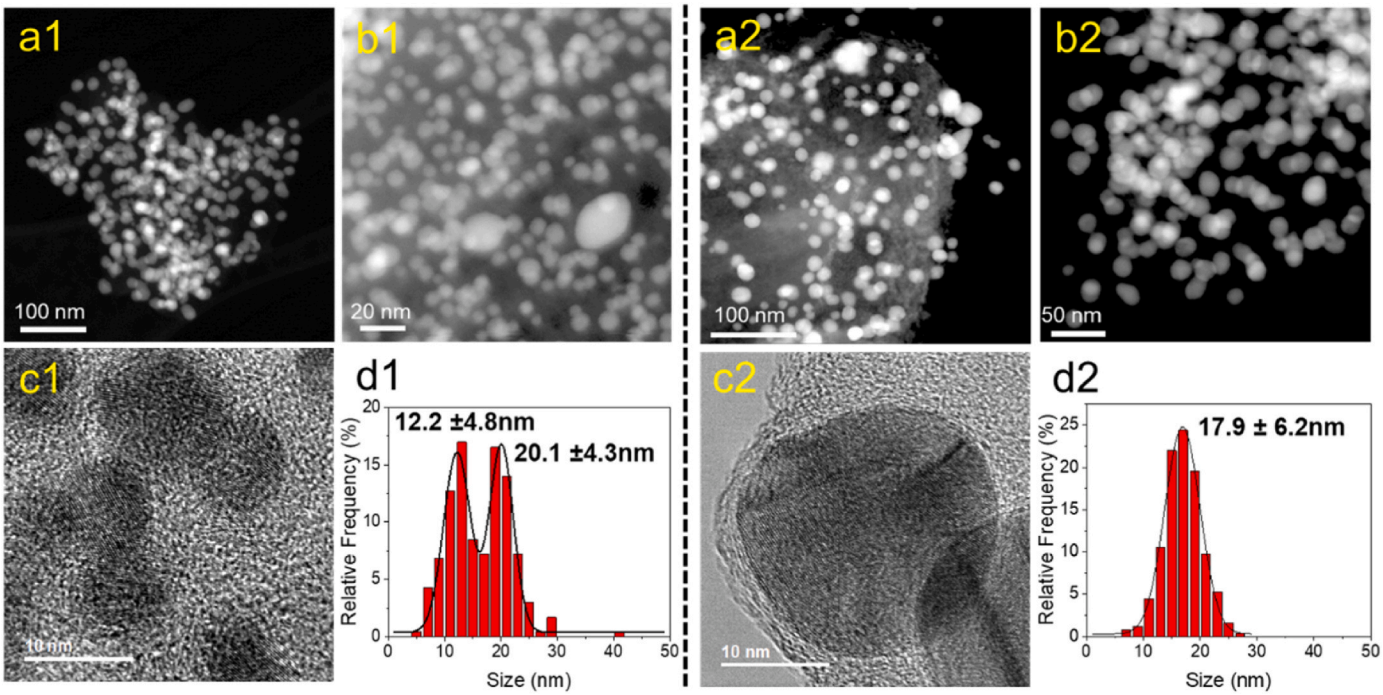

Fig. 6. Electron microscopy characterization of **PdCo-QT after OER** (left panel; 1) and **PdCo-QT after HER** (right panel; 2). (a) and (b) Representative HR-HAADF STEM images of the **PdCo-QT** catalyst, (c) Representative HR-TEM image of the **PdCo-QT** catalyst and, (d) nanoparticle size distribution.

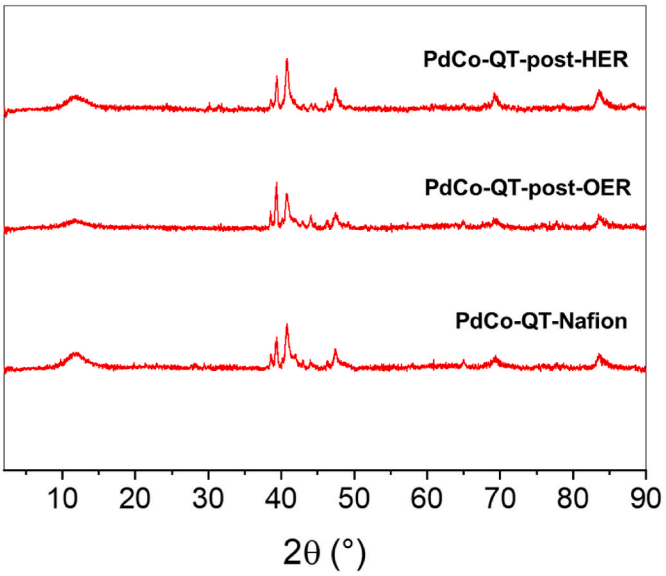

Fig. 7. XRD patterns of **PdMn-QT-Nafion**, and **PdMn-QT-Nafion** post OER and HER.

systems change. The peak and 39.4° corresponding to the (111) reflection planes of the cobalt-doped palladium $Pd_{0.9}Co_{0.1}$ phase showed a slightly higher intensity/width, suggesting the crystal growth during the OER process. This observation is confirmed by the crystal size estimated with the Scherrer equation, where the $Pd_{0.9}Co_{0.1}$ phase presents a bigger crystal size than that of the fresh material. Except for this last observation, the **PdCo-QT** electrodes reveal good stability toward the OER process and even greater stability toward the HER process.

Additionally, compositional analyses were performed on the resulting **PdCo-QT** material after OER and HER. Both **PdCo-QT-OER** and **PdCo-QT-HER** STEM XEDS studies (Figs. 8 and 9) confirmed the stability of the bimetallic nature of the PdCo nanoparticles. In that sense, the spectra evidence mixing at atomic scale of Pd and Co atoms, in good agreement with PXRD and TEM results. However, STEM-EELS studies revealed differences compared to the fresh material. In particular, after both OER and HER processes, where a disappearance of the C–O carbon layer is observed. Among other, this structural modification could explain the increase of the ESCA value thought a higher accessibility of the substrate to the actives centers.

Then, Fig. S10 presents the Pd*3d*XP region (Fig. S10b) after both HER and OER. The relative intensity ratio between the signals characteristic of $Pd^0 3d_{5/2}$ (ca. 335 eV) and surface oxidized Pd (ca. 337 eV) changes compared to the fresh electrodes. Thus, the palladium surface appeared more oxidized after both processes. Then, compared to the fresh electrode, the spectrum for C*1s* XP region (Fig. S10a) after HER and OER preserves the same components, but the components corresponding to Nafion have almost disappeared or were not detected. Again, in a similar way to the fresh PdCo-based electrode with Nafion, a defective or differentially charged carbon appears below 284 eV. Nevertheless, the carbon matrix of the electrodes appeared relatively stable through the catalytic processes. In the same line, in the N*1s* (Fig. S10c), the signal at ca. 400.7 eV remains after the electrocatalytic processes (i.e. HER and OER). Furthermore, Fig. 10a and Table S5 present and compare the Raman spectra of **PdCo-QT** electrodes after the oxygen evolution reaction (OER) and hydrogen evolution reaction (HER) to the fresh material. The spectra show remarkable similarity before and after electrocatalysis, indicating the stability of the carbon support. The typical graphitic carbon G band appears around 1589 cm^{-1}, with the I_D/I_G ratio suggesting a low order of carbon. However, the G and D band values slightly shift towards a higher Raman shift after catalysis, indicating minor modifications in the carbon composition [45,71]. As an explanation, this shift could be induced by the disappearance of the CO carbon layer detected early by EELS analysis [71,72]. Besides, the initial Raman spectrum of **PdCo-QT** is also characterized by two peaks at 631 cm^{-1} and 672 cm^{-1} typical of CoO_x species [43]. After HER and the reductive conditions it implies, the CoO_x species completely disappeared. However, after OER, additional peaks at 1027 cm^{-1} and 1285 cm^{-1} are detected, which could be attributed to the formation of novel **Co–O (OH)–Pd** bimetallic intersections during catalysis. To corroborate this

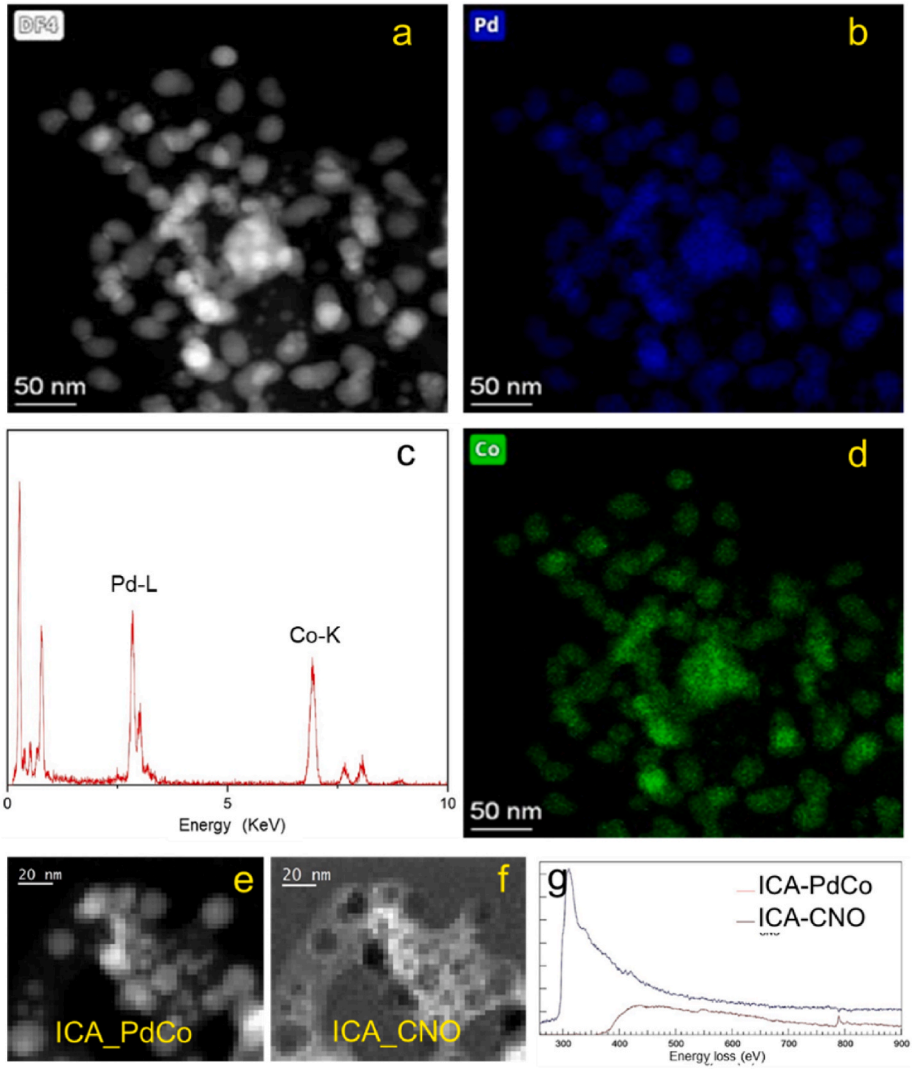

Fig. 8. STEM-XEDS and STEM-EELS of **PdCo-QT electrode after OER**. (a) HAADF image and the corresponding chemical maps extracted from the STEM–SI–XEDS: (b) Pd and (d) Co. (c) A representative XEDS spectrum. (g) EELS spectra with the two independent components, a Pd–Co component and, a C–N–O component (e), and (f) images corresponding to the three components of the ICA analysis of the whole set of STEM-EELS-SI data.

result, in-situ raman spectroelectrochemical measurements under OER conditions of the **PdCo-QT** and its monometallic counterpart **Pd-QT** were performed (Fig. S5a). For comparative purpose, the *operando* Raman spectra of the prototypical cobalt oxide and oxy-hydroxide pure phases deposited onto a graphite electrode were also measured (Fig. S5b). Notably, the Raman spectrum of monometallic **Pd-QT** material is solely characterized by the carbon G and D band of the support, suggesting that the Raman peaks observed **PdCo-QT** under OER conditions originates from the introduction of cobalt-palladium interaction metal. In addition, the observed two peaks at 631 cm^{-1} and 672 cm^{-1} are blue shifted compared to the main Raman bands characteristic of CoOOH and Co_3O_4 species, which can be also attributed to the C**o–O–Pd** interaction. Thus, the detected structural modifications mainly highlighted by Raman spectroscopy could explain the increase of the ECSA as well as the highest activity of the activated electrodes.

To strengthen the conclusions drawn from electron microscopy, PXRD, XPS, and Raman analyses, X-ray absorption spectroscopy (XAS) was employed to probe the electronic structure and local atomic environments of Pd and Co species within the bulk of the **PdCo-QT** electrode (Fig. 10). Pd (Fig. 10b) and Co (Fig. 10c) K-edge XANES spectra were collected at the ALBA synchrotron (NOTOS beamline) using a Nonlinear Spectro-EFC electrochemical flow cell (Redox.me), coupled to a PGSTAT202 potentiostat (Metrohm). The XANES operando measurements were performed under three conditions: (i) freshly prepared electrodes, (ii) after HER (−1.3 V, >30 min), and (iii) after OER (0.7 V, 30 min) all in 1 M KOH (*see SI, Section II-catalyst characterization XAS)*. As shown in Fig. 10b, the normalized Pd K-edge XANES spectrum of the fresh electrode closely matches that of Pd foil, with post-edge oscillations indicating metallic Pd ensembles. Minor spectral shifts and damping suggest interactions with neighboring Co atoms, consistent with prior findings [42]. Similarly, the Co K-edge XANES spectra (Fig. 10c) reveal deviations from the Co foil reference, indicative of the formation of bimetallic Pd–Co species. These features corroborate the Pd-edge analysis, supporting the existence of a stable bimetallic framework. Notably, the electronic structure and local geometry of both Pd and Co atoms remain largely unchanged throughout the catalytic process, reflecting the high structural stability of the **PdCo-QT** electrode. These results are in good agreement with previous characterizations. Due to the intrinsic bulk sensitivity of XAS, subtle changes at the nanoparticle surface where catalysis predominantly occurs and which accounts for only ~5 % of total atoms (*see SI, Section IICatalyst characterization XAS*) are not readily detectable [73,74]. Consequently, the EXAFS fitting results exhibit minimal variation across the different catalytic stages, as shown by the moduli of the Fourier transform and

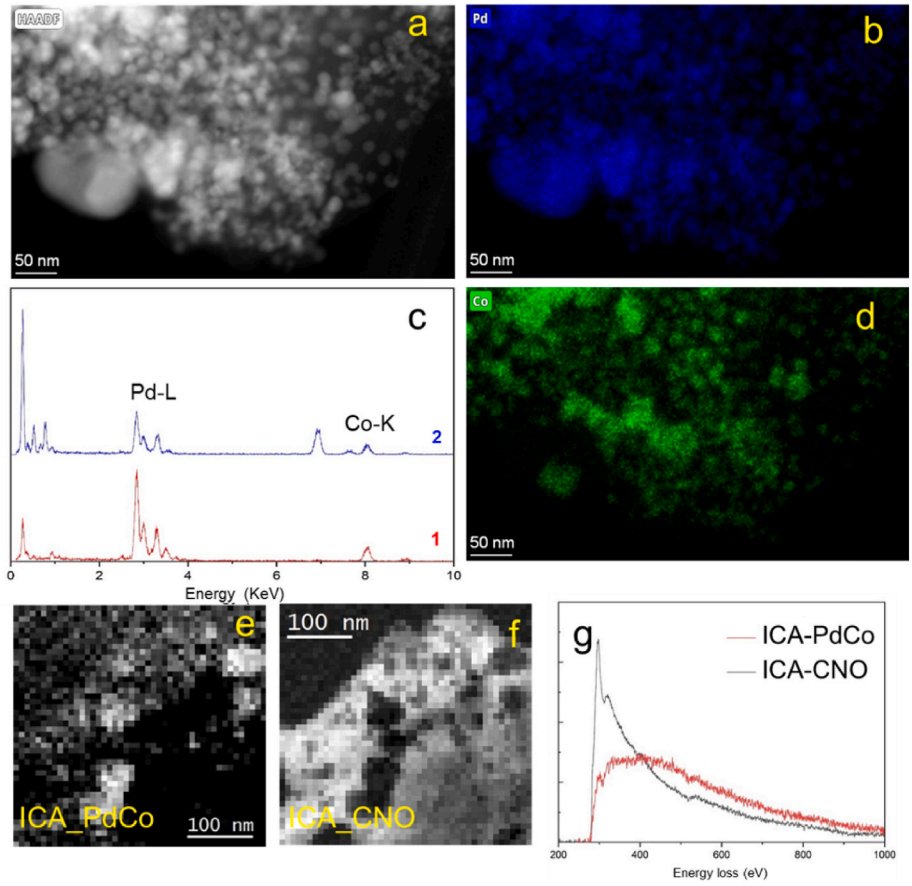

Fig. 9. STEM-XEDS and STEM-EELS of **PdCo-QT electrode after HER**. (a) HAADF image and the corresponding chemical maps extracted from the STEM–SI–XEDS: (b) Pd and (d) Co. (c) a representative XEDS spectrum. (g) EELS spectra with the three independent components, a Pd–Co component and, a C–N–O component. (e) and, (f) images corresponding to the three components of the ICA analysis of the whole set of STEM-EELS-SI data.

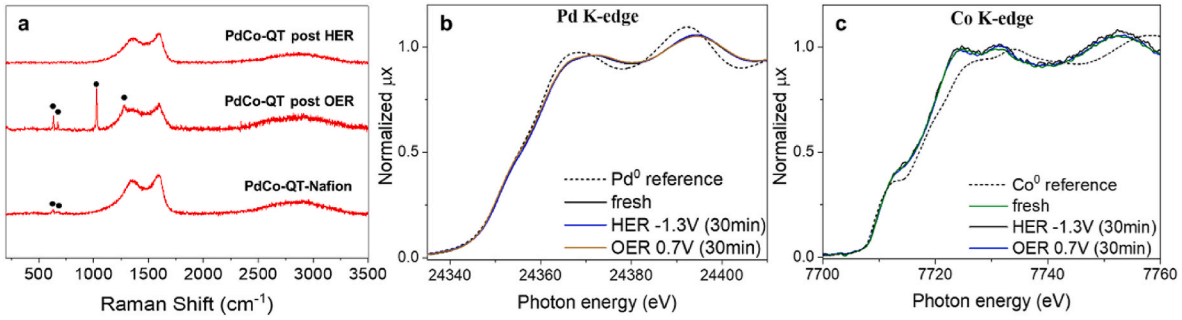

Fig. 10. (a) Raman and (b) XANES spectra at the Pd and (c) Co K-edges of **PdCo-QT-Nafion** electrode fresh and after OER (0.7 V, 30 min) and HER (−1.3 V, 30 min).

corresponding fits in Fig. S16. Fitting parameters are summarized in Table S8 and S9 and closely mirror those reported in our earlier study [42].

Based on these results, we can speculate that the superb electrocatalytic performance for HER and OER may arise from a synergistic electronic interaction between the metallic species of the material. Indeed, it is well recognized that direct interaction of a noble metal (d-electron number greater than d-orbital number) and a non-noble transition metal (with unpaired d-electrons and unfilled d-orbital) improve the catalytic activity of the precious metal by changing its charge distribution. Accordingly, a cobalt-induced partial charge transfer process can provoke a change of the average energy of the surface d-band that can modulate the adsorption energy of the catalytic species (hydrogen or oxygen intermediates), which ultimately enhances the electrocatalyst performance for water oxidation and reduction.

2.4. *Operational stability of the activated PdCo-QT-based electrodes*

To confirm the operational stability of the **PdCo-QT** modified electrodes, the OER or HER performances of freshly prepared electrodes were monitored for 3 days by performing RDE galvanostatic electrolysis at 1.67 V and −0.12 V, respectively, during 2 h per day (Fig. 11a and b). As can be observed, in both OER and HER processes, the catalytic current density gradually increases, in absolute value, during two pulses due to the activation of the catalyst, but slightly decreases resulting in a decrease of less than 10 % after three electrolysis. The long-term stability tests result in a total cumulative charge after the OER and HER experiments of 18.9C and 45.6C, respectively. Additionally, the OER

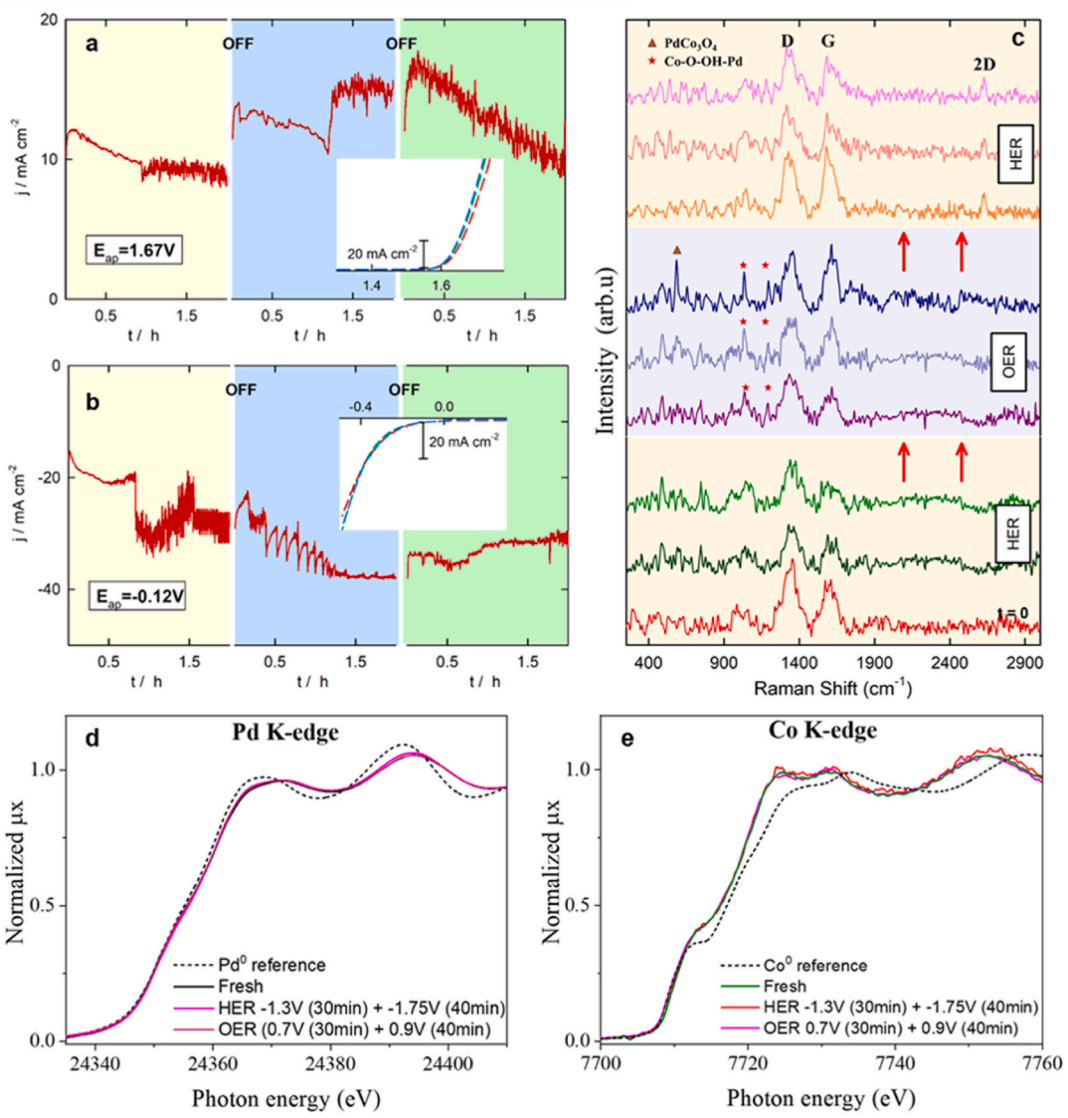

Fig. 11. (a) Chronoamperogram for a **PdCo-QT@Nafion** electrode for three on/off cycles recorded at 1.67 V and (b) −0.12 V vs. RHE. Inset plots: OER (panel *a*) and HER (panel *b*) polarization curves measured at 5 mV s^{-1} after each catalytic run. All measurements were carried out in a deaerated solution of KOH 1 M, at 25 °C. (c) Raman spectra of a **PdCo-QT@Nafion** electrode during consecutive HER-OER-HER electrolysis at the above-mentioned conditions. (d) XANES spectra at the Pd and (e) Co K-edges of **PdCo-QT@Nafion** electrode fresh and after OER (30 min at 0.7 V + 40 min at 0.9 V) and HER (−1.3V, 30 min at −1.3 V + 40 min at −1.75 V).

polarization curves recorded after each potential pulse (inset in Fig. 11a and b) reveal that the **PdCo-QT** electrode retains a remarkable electrocatalytic performance during 3 days. Besides, the stable electronic structure and local atomic environments of Pd and Co species within the bulk of the **PdCo-QT** electrode during an extended XAS operando experiment were recorded at Pd and Co edge after the applications of harsher OER and HER conditions (OER: 0.7 V for 30 min plus 0.9 V for 40 min and HER: 1.3 V for 30 min and −1.75 V for 40 min), revealing a superb reversibility of the material (Fig. 11d and e).

To support this result obtained by *ex-situ* XANES analysis, we also checked the functional reversibility of the catalysts by consecutive HER-OER-HER electrolysis tracking the evolution of the electronic structure and composition of **PdCo-QT** electrode using Raman *operando* experiments (*see SI*) (Fig. 11c). Particularly, the D, G and 2D typical carbon graphitic Raman signals are observable during the entire experiment around 1350, 1600 and 2600 cm^{-1}, respectively. In HER conditions, no evidence of CoO_x species was observed, which is consistent with the reductive atmosphere provided by the reaction. However, in the OER conditions, typical peaks from shifted CoO_x species appeared. The reversibility of the shifted CoO_x species formation and the similar band positions observed by the operando and ex-situ analysis converge towards the formation at surface level of novel **Co–O(OH)–Pd** bimetallic intersections during catalysis thus explaining the high activity of our **PdCo-QT** electrode.

Finally, we have evaluated the stability of the optimum **PdCo-QT** material as bifunctional catalyst for the overall water splitting at alkaline medium. For this purpose, we used a separated two-compartment H-type alkaline electrolyzer setup consisting of electrodes of carbon Toray modified with a catalytic ink containing the **PdCo-QT@Nafion** composite (*see SI Section IV Additional Electrochemical Characterization*). The operational performance of the **PdCo-QT** || **PdCo-QT** electrolyzer was tested by monitoring the evolution of their polarization curves along a chronopotentiometric electrolysis at 0.13 A during ca. 24 h. (Fig. S6). It is observed that the initial cell voltage of 2.5 V progressively increase along the first 10 h of electrolysis, reaching a value of ~ 2.90 V. Then, the cell voltage was found to remain almost unchanged until the end of the electrolysis, suggesting that the material remain stable after a conditioning time. Similar conclusions can be extracted from the evolution of the polarization curves during the experiments.

3. Conclusions

Recently, we presented the soft chemical transformation followed by a pyrolysis step of a new **PdCo-MOF** and **PdMn-MOF** resulting in the formation of Co/Mn-doped Pd nanoparticles (Pd-NPs) supported on nitrogen-doped graphitic carbon, creating materials with well-defined and distributed particles. Remarkably, the present work reports the successful use of these materials to construct electrodes for boosting the electrocatalytic hydrogen evolution reaction (HER) and oxygen evolution reaction (OER), demonstrating significantly enhanced electrocatalytic performance with respect to its monometallic counterpart with improved catalytic metrics in terms of overpotential at high current densities, high mass activity, and superior stability. The electrodes were subjected to a deep characterization study including HR-EM, PXRD, RAMAN and XPS. Notably, the Co-doped material yields the lowest slope (70 mV dec^{-1}) in comparison to 145 mV dec^{-1} and 185 mV dec^{-1} for Mn-doped materials and monometallic Pd nanoparticles in the HER process, respectively. In OER, Pd, PdCo and PdMn, nanoparticles display Tafel slopes of 110 mV dec^{-1}, 75 mV dec^{-1} and 100 mV dec^{-1}, respectively. Excitingly, the performance of the **PdCo-QT-based** electrode competes with that of benchmark catalytic materials for these reactions, indicating a positive synergistic effect arising from its multimetallic nature. This effect is attributed to the strong interactions between Pd and M (M = Co, Mn), likely forming **Pd–O(OH)–Co** active centers. Furthermore, the impressive electrocatalytic performance and stability demonstrated by deep operando and ex-situ characterizations of an electrolytic cell using two electrodes containing the bimetallic **PdCo-QT** composites suggests its high potential for practical water-splitting applications.

CRediT authorship contribution statement

Jordan Santiago Martinez: Writing – review & editing, Writing – original draft, Investigation, Formal analysis. **Inmaculada Márquez:** Writing – review & editing, Writing – original draft, Investigation, Formal analysis. **Jaime Mazarío:** Writing – review & editing, Writing – original draft, Methodology, Investigation, Formal analysis. **Christian Wittee Lopes:** Writing – original draft, Investigation. **Christian Cerezo-Navarrete:** Writing – original draft, Investigation. **Gonzalo Egea:** Investigation. **Giovanni Agostini:** Writing – original draft. **Eduardo Villalobos-Portillo:** Writing – review & editing, Writing – original draft. **Otman Bazta:** Investigation. **Susana Trasobares:** Writing – original draft. **Jose Juan Calvino:** Writing – review & editing, Writing – original draft, Funding acquisition. **Juan José Calvente:** Writing – review & editing, Writing – original draft. **José Luis Olloqui-Sariego:** Writing – review & editing, Writing – original draft, Supervision, Investigation, Funding acquisition. **Pascual Oña-Burgos:** Writing – review & editing, Writing – original draft, Supervision, Funding acquisition, Conceptualization.

Notes

The authors declare no competing financial interest.

Declaration of competing interest

The authors declare that they have no known competing financial interests or personal relationships that could have appeared to influence the work reported in this paper.

Aknowledgments

Financial support by Severo Ochoa center of excellence program (CEX2021-001230-S) is gratefully acknowledged. The authors thank the financial support from the Spanish Government (PID2022-140111OB-I00, PID2021-126799NB-I00, TED2021-130191B–C41, TED2021-130191B–C42, and TED2021-130191B–C44 funded by MCIN/AEI/10.13039/501100011033 and European Union Next Generation EU/PRTR). This study forms part of the Advanced Materials program and was supported by MCIN with partial funding from European Union Next Generation EU (PRTR-C17. I1) and by Generalitat Valenciana (MFA/2022/047). In addition, this work has received funding from the European Union's Horizon 2020 research and innovation program under grant agreement No 101022507. C.W.L. acknowledges the National Council for Scientific and Technological Development – CNPq/Brazil (443418/2023–3) and PPGQ-UFPR for financial support. HR-STEM studies were performed at the DME-UCA node of the ELECMI Spanish Unique Infrastructure (ICTS) for Electron Microscopy of Materials. Some of these experiments were performed NOTOS beamlines at ALBA Synchrotron with the collaboration of ALBA staff (Carlos Escudero, and Carlo Marini).

Appendix A. Supplementary data

Supplementary data to this article can be found online at https://doi.org/10.1016/j.ijhydene.2025.152565.

References

[1] Zhang H, Zhou W, Dong J, Lu XF, Lou XW. David). Intramolecular electronic coupling in porous iron cobalt (oxy)phosphide nanoboxes enhances the electrocatalytic activity for oxygen evolution. Energy Environ Sci 2019;12:3348–55.
[2] Sathre R, Greenblatt JB, Walczak K, Sharp ID, Stevens JC, Ager JW, et al. Opportunities to improve the net energy performance of photoelectrochemical water-splitting technology. Energy Environ Sci 2016;9:803–19.
[3] Yin Tee S, Yin Win K, Siang Teo W, Koh L-D, Liu S, Peng Teng C, et al. Recent progress in energy-driven water splitting. Adv Sci 2017;4:1600337.
[4] Xiang C, Papadantonakis KM, Lewis NS. Principles and implementations of electrolysis systems for water splitting. Mater Horiz 2016;3:169–73.
[5] Xu Y, Zhang B. Recent advances in electrochemical hydrogen production from water assisted by alternative oxidation reactions. Chemelectrochem 2019;6:3214–26.
[6] Zhang J, Zhao Z, Xia Z, Dai L. A metal-free bifunctional electrocatalyst for oxygen reduction and oxygen evolution reactions. Nat Nanotechnol 2015;10:444–52.
[7] Seh ZW, Kibsgaard J, Dickens CF, Chorkendorff I, Nørskov JK, Jaramillo TF. Combining theory and experiment in electrocatalysis: insights into materials design. Science 2017;355.
[8] Tiwari JN, Nath K, Kumar S, Tiwari RN, Kemp KC, Le NH, et al. Stable platinum nanoclusters on genomic DNA–Graphene oxide with a high oxygen reduction reaction activity. Nat Commun 2013;4:1–7.
[9] Li L, Chang Z wen, Zhang XB. Recent progress on the development of metal-air batteries. Adv Sustain Syst 2017;1:1700036.
[10] Xia BY, Yan Y, Li N, Wu H Bin, Lou XWD, Wang X. A metal–organic framework-derived bifunctional oxygen electrocatalyst. Nat Energy 2016;1:1–8.
[11] Ma TY, Dai S, Jaroniec M, Qiao SZ. Metal–organic framework derived hybrid Co3O4-Carbon porous nanowire arrays as reversible oxygen evolution electrodes. J Am Chem Soc 2014;136:13925–31.
[12] Piccinin S, Sartorel A, Aquilanti G, Goldoni A, Bonchio M, Fabris S. Water oxidation surface mechanisms replicated by a totally inorganic tetraruthenium-oxo molecular complex. Proc Natl Acad Sci U S A 2013;110:4917–22.
[13] Yin Q, Tan JM, Besson C, Geletii YV, Musaev DG, Kuznetsov AE, et al. A fast soluble carbon-free molecular water oxidation catalyst based on abundant metals. Science 2010;328:342–5.
[14] Morales-Guio CG, Stern L-A, Hu X. Nanostructured hydrotreating catalysts for electrochemical hydrogen evolution. Chem Soc Rev 2014;43:6555–69.
[15] Bai S, Wang C, Deng M, Gong M, Bai Y, Jiang J, et al. Surface polarization matters: enhancing the hydrogen-evolution reaction by shrinking Pt shells in pt–pd–graphene stack structures. Angew Chem Int Ed 2014;53:12120–4.
[16] Su C, Yang T, Zhou W, Wang W, Xu X, Shao Z. Pt/C–LiCoO2 composites with ultralow Pt loadings as synergistic bifunctional electrocatalysts for oxygen reduction and evolution reactions. J Mater Chem A 2016;4:4516–24.
[17] Tian J, Liu Q, Asiri AM, Sun X. Self-supported nanoporous cobalt phosphide nanowire arrays: an efficient 3D hydrogen-evolving cathode over the wide range of pH 0–14. J Am Chem Soc 2014;136:7587–90.
[18] She ZW, Kibsgaard J, Dickens CF, Chorkendorff I, Nørskov JK, Jaramillo TF. Combining theory and experiment in electrocatalysis: insights into materials design. Science 2017;355.
[19] Bezerra LS, Maia G. Developing efficient catalysts for the OER and ORR using a combination of Co, Ni, and Pt oxides along with graphene nanoribbons and NiCo2O4. J Mater Chem A 2020;8:17691–705.
[20] Wu X, Tang C, Cheng Y, Min X, Jiang SP, Wang S. Bifunctional catalysts for reversible oxygen evolution reaction and oxygen reduction reaction. Chem Eur J 2020;26:3906–29.

[21] Du X, Ding Y, Zhang X. Selectively Se-doped Co3O4@CeO2 nanoparticle-dotted nanoneedle arrays for high-efficiency overall water splitting. Appl Surf Sci 2021; 562:150227.
[22] Du X, Zhang C, Wang H, Wang Y, Zhang X. Controlled synthesis of Co9S8@ NiCo2O4 nanorod arrays as binder-free electrodes for water splitting with impressive performance. J Alloys Compd 2021;885:160972.
[23] Dai Z, Du X, Wang Y, Han X, Zhang X. Promoting urea oxidation and water oxidation through interface construction on a CeO2@CoFe2O4 heterostructure. Dalton Trans 2021;50:12301–7.
[24] Akbari N, Kondov I, Vandichel M, Aleshkevych P, Najafpour MM. Oxygen-evolution reaction by a palladium foil in the presence of iron. Inorg Chem 2021;60: 5682–93.
[25] Chung DY, Lopes PP, Farinazzo Bergamo Dias Martins P, He H, Kawaguchi T, Zapol P, et al. Dynamic stability of active sites in hydr(oxy)oxides for the oxygen evolution reaction. Nat Energy 2020;5:222–30.
[26] Garcia AC, Touzalin T, Nieuwland C, Perini N, Koper MTM. Enhancement of oxygen evolution activity of nickel oxyhydroxide by electrolyte alkali cations. Angew Chem Int Ed 2019;58:12999–3003.
[27] Chaturvedi P, Sarker S, Chen X, Das S, Luo H, Smirnov SN. Enhancing the cooperative catalytic effect in Ni/Co Hydr(oxy)oxide porous electrodes for overall water splitting and glucose sensing. ACS Sustainable Chem Eng 2019;7:11303–12.
[28] Gong L, Yang H, Douka AI, Yan Y, Xia BY. Recent progress on NiFe-Based electrocatalysts for alkaline oxygen evolution. Adv Sustain Syst 2021;5:2000136.
[29] Liu S, Chen T, Ying H, Li Z, Hao J. Deep eutectic solvent-mediated construction of oxygen vacancy-rich Fe-Based electrocatalysts for efficient oxygen evolution reaction. Adv Sustain Syst 2020;4:2000038.
[30] Maiti K, Balamurugan J, Peera SG, Kim NH, Lee JH. Highly active and durable core-shell fct-PdFe@Pd nanoparticles encapsulated NG as an efficient catalyst for oxygen reduction reaction. ACS Appl Mater Interfaces 2018;10:18734–45.
[31] Martinez J, Mazarío J, Luis Olloqui-Sariego J, José Calvente J, Darawsheh MD, Mínguez-Espallargas G, et al. Bimetallic intersection in PdFe@FeOx-C nanomaterial for enhanced water splitting electrocatalysis. Adv Sustain Syst 2022; 6:2200096.
[32] Radwan A, Jin H, He D, Mu S. Design engineering, synthesis protocols, and energy applications of MOF-Derived electrocatalysts. Nano-Micro Lett 2021;13:1–32.
[33] Su R, Wang R, Wang H, Liu Y, Yan Y, Yin H, et al. A biomass-modified carbon nitride composite electrode for photoelectrocatalytic enhancement of overall water splitting. Int J Hydrogen Energy 2025;117:24–38.
[34] Yin H, An Y, Li C, Yan Y, Su R, Wan C, et al. Heteroatom-doped, vinegar residue-derived fluorine/chlorine Co-doped vertical graphene-supported carbon quantum dots as high-efficiency all-carbon electrodes for water electrolysis hydrogen production. J Environ Chem Eng 2025;13:117654.
[35] Jiang B, Tian Y, An Y, Liu R, Shaik F. Electrocatalytic activity analysis of vinegar residue-based heteroatom-doped carbon quantum dots integrated on vertically aligned graphene arrays for hydrogen evolution reaction. Int J Hydrogen Energy 2023;48:38686–98.
[36] Bavykina A, Kolobov N, Khan IS, Bau JA, Ramirez A, Gascon J. Metal-organic frameworks in heterogeneous catalysis: recent progress, new trends, and future perspectives. Chem Rev 2020;120:8468–535.
[37] Wang HF, Chen L, Pang H, Kaskel S, Xu Q. MOF-derived electrocatalysts for oxygen reduction, oxygen evolution and hydrogen evolution reactions. Chem Soc Rev 2020;49:1414–48.
[38] Liang Z, Qiu T, Gao S, Zhong R, Zou R, Liang Z, et al. Multi-scale design of metal–organic framework-derived materials for energy electrocatalysis. Adv Energy Mater 2022;12:2003410.
[39] Hou C-C, Xu Q, Hou C-C, Xu Q. Metal–organic frameworks for energy. Adv Energy Mater 2019;9:1801307.
[40] Darawsheh MD, Mazarío J, Lopes CW, Giménez-Marqués M, Domine ME, Meira DM, et al. MOF-mediated synthesis of supported Fe-Doped Pd nanoparticles under mild conditions for magnetically recoverable catalysis**. Chem Eur J 2020; 26:13659–67.
[41] Martinez JS, Mazarío J, Lopes CW, Trasobares S, Calvino Gamez JJ, Agostini G, et al. Efficient alkyne semihydrogenation catalysis enabled by synergistic chemical and thermal modifications of a PdIn MOF. ACS Catal 2024;14:4768–85.
[42] Martinez JS, Carpisassi L, Egea G, Mazarío J, Lopes CW, Mora-Moreno C, et al. MOF-derived PdCo and PdMn systems as versatile catalysts in alkyne semihydrogenation. ACS Catal 2025:7263–82.
[43] Yang J, Liu H, Martens WN, Frost RL. Synthesis and characterization of Cobalt hydroxide, cobalt oxyhydroxide, and cobalt oxide nanodiscs. J Phys Chem C 2010; 114:111–9.
[44] Ferrari AC, Robertson J. Interpretation of Raman spectra of disordered and amorphous carbon. Phys Rev B 2000;61:14095.
[45] Li Z, Deng L, Kinloch IA, Young RJ. Raman spectroscopy of carbon materials and their composites: Graphene, nanotubes and fibres. Prog Mater Sci 2023;135: 101089.
[46] Martínez de Yuso MV, Calderón AB, Romero V, Cuberes MT, Benavente J. Chemical and homogeneity changes of a nafion membrane surface associated to its doping with the cation of the room-temperature ionic liquid AliquatCl. Surf Interface Anal 2016;48:561–5.
[47] Dzara MJ, Artyushkova K, Foster J, Eskandari H, Chen Y, Mauger SA, et al. X-ray Photoelectron spectroscopy analysis of nafion-containing samples: pitfalls, protocols, and perceptions of physicochemical properties. J Phys Chem C 2024; 128:8467–82.
[48] Barinov A, Malcioğlu OB, Fabris S, Sun T, Gregoratti L, Dalmiglio M, et al. Initial stages of oxidation on graphitic surfaces: photoemission study and density functional theory calculations. J Phys Chem C 2009;113:9009–13.
[49] Moddeman WE, Bowling WC, Carter DC, Grove DR. XPS surface and bulk studies of heat treated palladium in the presence of hydrogen at 150°C. Surf Interface Anal 1988;11:317–26.
[50] Shafeev GA, Themlin J-M, Bellard L, Marine W, Cros A. Enhanced adherence of area-selective electroless metal plating on insulators. J Vac Sci Technol A 1996;14: 319–26.
[51] NIST X-ray Photoelectron Spectroscopy (XPS) Database, Version 3.5 n.d. https ://srdata.nist.gov/xps/.
[52] Artyushkova K. Misconceptions in interpretation of nitrogen chemistry from x-ray photoelectron spectra. J Vac Sci Technol A 2020;38:31002.
[53] Major GH, Fairley N, Sherwood PMA, Linford MR, Terry J, Fernandez V, et al. Practical guide for curve fitting in x-ray photoelectron spectroscopy. J Vac Sci Technol A 2020;38:61203.
[54] Vidal M, Dehaghani MS, Yoshii T, Wakabayashi K, Cameán I, Barreau M, et al. Probing Prismatic/Basal surfaces of carbon materials upon graphitization by gas adsorption, TPD, and XPS. J Phys Chem C 2024;128(44):18993–9012.
[55] Blume R, Rosenthal D, Tessonnier JP, Li H, Knop-Gericke A, Schlögl R. Characterizing graphitic carbon with X-ray Photoelectron spectroscopy: a step-by-step approach. ChemCatChem 2015;7:2871–81.
[56] Ipadeola AK, Ozoemena KI. Alkaline water-splitting reactions over Pd/Co-MOF-derived carbon obtained via microwave-assisted synthesis. RSC Adv 2020;10: 17359–68.
[57] Bhowmik T, Kundu MK, Barman S. Palladium nanoparticle-graphitic carbon nitride porous synergistic catalyst for hydrogen evolution/oxidation reactions over a broad range of pH and correlation of its catalytic activity with measured hydrogen binding energy. ACS Catal 2016;6:1929–41.
[58] Sheng W, Myint M, Chen JG, Yan Y. Correlating the hydrogen evolution reaction activity in alkaline electrolytes with the hydrogen binding energy on monometallic surfaces. Energy Environ Sci 2013;6:1509–12.
[59] Lasia A. Mechanism and kinetics of the hydrogen evolution reaction. Int J Hydrogen Energy 2019;44:19484–518.
[60] Pluntke Y, Kibler LA. Hydrogen evolution electrocatalysis on AgPd(111) alloys. Electrocatalysis 2011;2:192–9.
[61] Lasia A. On the mechanism of the hydrogen absorption reaction. J Electroanal Chem 2006;593:159–66.
[62] Iwakura C, Matsuoka M, Kohno T. Mixing effect of metal oxides on negative electrode reactions in the Nickel-Hydride battery. J Electrochem Soc 1994;141: 2306–9.
[63] Mahmood N, Yao Y, Zhang JW, Pan L, Zhang X, Zou JJ. Electrocatalysts for hydrogen evolution in alkaline electrolytes: mechanisms, challenges, and prospective solutions. Adv Sci 2018;5:1700464.
[64] Sheng W, Zhuang Z, Gao M, Zheng J, Chen JG, Yan Y. Correlating hydrogen oxidation and evolution activity on platinum at different pH with measured hydrogen binding energy. Nat Commun 2015;6:1–6.
[65] Danilovic N, Subbaraman R, Strmcnik D, Chang K-C, Paulikas AP, Stamenkovic VR, et al. Enhancing the alkaline hydrogen evolution reaction activity through the bifunctionality of Ni(OH)2/Metal catalysts. Angew Chem 2012;124:12663–6.
[66] Quaino P, Juarez F, Santos E, Schmickler W. Volcano plots in hydrogen electrocatalysis – uses and abuses. Beilstein J Nanotechnol 2014;5:846–54.
[67] Shen F, Wang Y, Qian G, Chen W, Jiang W, Luo L, et al. Bimetallic iron-iridium alloy nanoparticles supported on nickel foam as highly efficient and stable catalyst for overall water splitting at large current density. Appl Catal B Environ 2020;278: 119327.
[68] Miller EL, Rocheleau RE. Electrochemical behavior of reactively sputtered iron-doped nickel oxide. J Electrochem Soc 1997;144:3072–7.
[69] McCrory CCL, Jung S, Peters JC, Jaramillo TF. Benchmarking heterogeneous electrocatalysts for the oxygen evolution reaction. J Am Chem Soc 2013;135: 16977–87.
[70] Lazanas AC, Prodromidis MI. Electrochemical impedance spectroscopy—a tutorial. ACS Meas Sci Au 2023;3:162–93.
[71] Chowdhury AKMS, Cameron DC, Hashmi MSJ. Vibrational properties of carbon nitride films by Raman spectroscopy. Thin Solid Films 1998;332:62–8.
[72] Bulusheva LG, Okotrub AV, Kinloch IA, Asanov IP, Kurenya AG, Kudashov AG, et al. Effect of nitrogen doping on Raman spectra of multi-walled carbon nanotubes. Phys Status Solidi 2008;245:1971–4.
[73] Agostini G, Piovano A, Bertinetti L, Pellegrini R, Leofanti G, Groppo E, et al. Effect of different face centered cubic nanoparticle distributions on particle size and surface area determination: a theoretical study. J Phys Chem C 2014;118:4085–94.
[74] Agostini G, Pellegrini R, Leofanti G, Bertinetti L, Bertarione S, Groppo E, et al. Determination of the particle size, available surface area, and nature of exposed sites for silica-alumina-supported Pd nanoparticles: a multitechnical approach. J Phys Chem C 2009;113:10485–92.